Laser-written micro-channel atomic magnetometer

Andrea Zanoni,[1,2] Kostas Mouloudakis,[3] Michael C. D. Tayler,[3] Giacomo Corrielli,[2] Roberto Osellame,[2] Morgan W. Mitchell,[3,4] and Vito Giovanni Lucivero[3,5]

[1)] *Dipartimento di Fisica — Politecnico di Milano, Piazza Leonardo da Vinci 32, 20133 Milano, Italy*

[2)] *Istituto di Fotonica e Nanotecnologie (IFN) — Consiglio Nazionale delle Ricerche (CNR), Piazza Leonardo da Vinci 32, 20133 Milano, Italy*

[3)] *ICFO - Institut de Ciències Fotòniques, The Barcelona Institute of Science and Technology, 08860 Castelldefels (Barcelona), Spain*

[4)] *ICREA - Institució Catalana de Recerca i Estudis Avançats, 08010 Barcelona, Spain*

[5)] *Dipartimento Interateneo di Fisica, Universitá degli Studi di Bari Aldo Moro, 70126 Bari, Italy*

(Dated: 23 April 2024)

We demonstrate a sensitive optically-pumped magnetometer using rubidium vapor and 0.75 amg of nitrogen buffer gas in a sub-mm-width sensing channel excavated by femtosecond laser writing followed by chemical etching. The channel is buried less than 1 mm below the surface of its fused silica host material, which also includes reservoir chambers and micro-strainer connections, to preserve a clean optical environment. Using a zero-field-resonance magnetometry strategy and a sensing volume of 2.25 mm^3, we demonstrate a sensitivity of $\approx 1\,pT/\sqrt{Hz}$ at 10 Hz. The device can be integrated with photonic structures and microfluidic channels with 3D versatility. Its sensitivity, bandwidth and stand-off distance will enable detection of localized fields from magnetic nanoparticles and µL NMR samples.

Microfabricated atomic vapor cells are used in miniaturized atomic devices including frequency references[1], clocks[2], gyroscopes[3], Rydberg-atom electrometers[4] and optically pumped magnetometers (OPMs)[5,6]. In most such devices, the miniaturized cells have mm or larger internal vapor dimensions[7]. As a rule, larger cell volumes enable better sensitivity but also impose a larger standoff distance from a source to the atoms measuring it[6]. Measurement of highly localized magnetic fields produced by sources, e.g., micro- or nano-scale electronics, microfluidic nuclear magnetic resonance (NMR) ensembles[8–10], micro-scale biomagnetism[11,12] or magnetic micro-and nano-particles[13,14], could benefit from a monolithic microfluidic platform with sub-mm-internal-dimension atomic and fluidic channels. This "lab-on-chip" approach to magnetic sensing has been studied with NV-centers[15,16], and demonstrated tens-of-$\mu T/\sqrt{Hz}$ sensitivities with nm and µm-scale sample sizes. With atomic vapors, the microfluidic approach has the potential to reach sub-$pT/\sqrt{Hz}$ sensitivities with mm-scale samples[17].

One proven technique for making both micro-fluidic devices[18–20] and atomic vapor cells with arbitrary internal geometries[21] is FLICE (Femtosecond Laser Irradiation followed by Chemical Etching)[22,23]. This technique exploits the nonlinear interaction between glass and focused ultrafast laser pulses to locally increase the material's susceptibility to wet etching processes. FLICE can generate three-dimensional empty channels with arbitrary geometry and micrometric resolution, buried in optical materials such as fused silica. FLICE is moreover compatible with laser-writing of optical waveguides and other optical elements. The combination of these techniques creates a route to integrated devices that simultaneously control optical, fluidic, and atomic elements in a single miniaturized package[24,25].

Prior work has used FLICE to produce a miniaturized vapor cell with a 1 mm × 1 mm cross section and 9.5 mm vapor length, with a buffer gas density of $\approx 5 \times 10^{-3}$ amg[21]. Due to the low pressure, this cell showed Doppler-free saturated-absorption resonances, of interest for laser frequency stabilization, but also low spin coherence time due to rapid diffusion to the walls and weak optical pumping efficiency, due to radiation trapping[21]. Here we demonstrate a FLICE-made miniaturized vapor cell with a 500 µm × 500 µm cross-section and 0.75 amg of N_2 buffer gas. This higher pressure allows us to study the potential of FLICE-made cells for sensitive magnetometry.

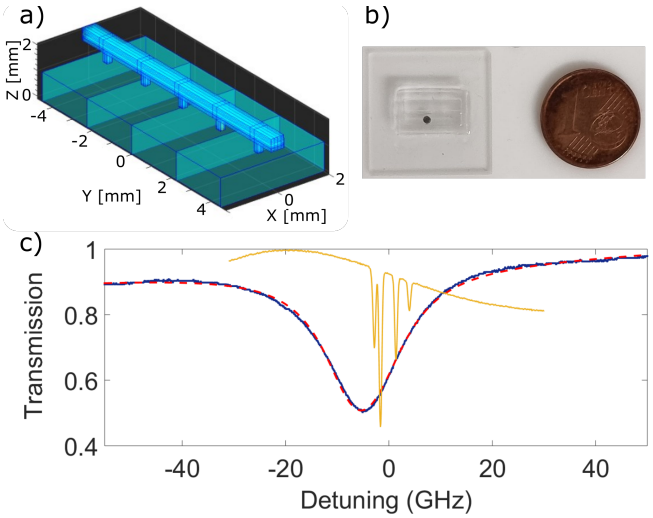

FIG. 1. a) Design of the LWVC with a bottom reservoir and a top 9 mm-long sensing micro-channel. b) LWVC after fabrication by FLICE, filling with a Rb solid state dispenser and sealing by UV-curing adhesive. c) Normalized transmission (blue) through the LWVC and fit (dashed red) to an absorptive Lorentzian plus a linear dependence on the DBR laser frequency. Simultaneous transmission through a Rb reference vapor cell (yellow) evacuated to 10^{-8} Torr.

The FLICE process, including filling and bonding steps for the fabrication of laser-written vapor cells (LWVCs), is described in detail in our prior work[21]. In this experiment we use a commercial femtosecond laser (CARBIDE - Light Conversion) to write the desired geometry into a 20 mm × 20 mm

fused silica slab with a thickness of 3 mm. As illustrated in Fig. 1(a) the laser-written geometry consists of a sensing micro-channel of length $l_{\mathrm{LWVC}} = 9$ mm and side $d_{\mathrm{LWVC}} = 500\,\mu$m with a square cross section. The distance between the void micro-channel and the silica top surface, which determines the stand-off distance from a potential sample on the top of the on-chip OPM, is 750 µm and could be reduced to few tens of microns. A 4 mm× 8 mm× 1 mm bottom reservoir, open at one end, is connected to the top physics channel by five 250 µm-wide "micro strainer" conduits. This configuration has been designed to give sub-mm confinement of the atomic ensemble over two dimensions with the potential of a sub-mm stand-off distance from a sample, while maintaining high optical depth due to the 9 mm interaction length. The etching process took about 10 h in hydrofluoric acid (HF) at 20 % concentration, at 35 °C, with the acid entering from the open reservoir and reaching the sensing channel to remove the modified material after irradiation and to obtain the final hollow micro structure. Filling and bonding steps have been performed inside a N_2-filled glove-box at atmospheric pressure. We first placed a dispenser of non-evaporable getter (NEG) material (SAES Getters RB/AMAX/PILL/1-0.6) in the cell reservoir. Then, we used UV-curing epoxy (Norland Products NOA61) to bond the cell to a square fused silica plate of dimensions 20 mm × 20 mm × 1 mm.[26] A picture of the final cell filled with the Rb dispenser is shown Fig. 1(b). The activation was performed for 20 s with a 5 W beam of cw light at 1064 nm, reaching the dispenser with a 200 µm waist from the top of the cell. A distributed Bragg reflector (DBR) probe laser was scanned around the center of the D_2 line of ^{85}Rb and detected after transmission through the physics channel to simultaneously monitor the activation by absorption spectroscopy. In Fig. 1(c) we show the absorption spectrum acquired with the cell stabilized at 90 °C for 2 h after activation. The absorption spectrum is fitted to a Lorentzian profile to obtain a full-width half maximum (FWHM) pressure-broadened linewidth of 13.5 GHz, corresponding to $\eta = 0.75$ amg of N_2[27]. This residual pressure simultaneously matches two requirements for efficient optical pumping[28] and high sensitivity optical magnetometry: the N_2 works as a quenching gas to avoid radiation trapping[29] and as a buffer gas to reduce the rate of depolarizing collisions of the Rb atoms with the cell walls[21,30]. A fine pressure tuning with resolution as low as 1 Torr has also been recently demonstrated in a micro-fabricated vapor cell[31] using cesium (Cs) dispensers, making the described filling and activation process suitable for chip-scale atomic sensors with different target pressures.

We use the LWVC to implement a zero-field resonance (ZFR) OPM[32–34]. The experimental setup is shown in Fig. 2(a). The light from a 795 nm DBR diode laser, resonant with the D_1 line of ^{87}Rb, is fiber-coupled in a single-mode fiber, whose output is aligned to pass through the atomic sensing channel of the LWVC in the z-direction. A half waveplate (HWP) and a polarizing beam splitter (PBS) are used to control the laser power and a zero-order quarter waveplate (QWP) to convert linear into circular polarization before atomic interaction. A spherical lens (not shown) with 100 mm focal length is used to shape the laser beam to have a waist of 250 µm at the

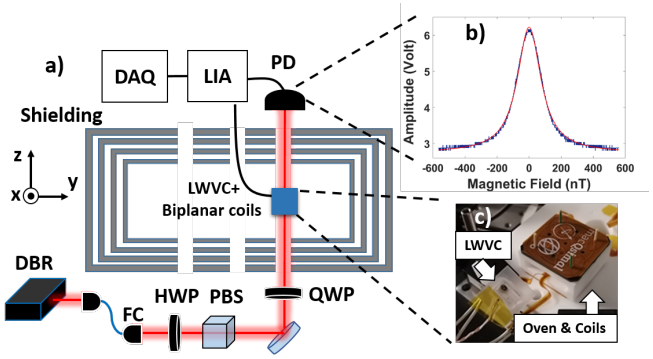

FIG. 2. a) Experimental setup for optical magnetometry. DBR - distributed Bragg reflector laser; FC - Fiber collimator; HWP- half wavepate; PBS - polarizing beam splitter; QWP - quarter waveplate; LWVC - laser-written vapor cell; PD - photodetector; LIA - lock-in amplifier; DAQ - data acquisition system. b) Zero-field resonance (ZFR) signal measured in transmission when a magnetic field is swept around zero in the x-direction, transvese to the laser beam propagation direction z. c) The system comprising the LWVC, a ceramic oven, a teflon insulator, and the biplanar coils. The module is placed within 4 layers of mu-metal magnetic shielding.

center of the LWVC. The cell was placed in a ceramic oven, heated through ac current at 40 kHz through flex-PCB resistive heater traces attached to the ceramic box. The setup is thermally insulated using a Teflon enclosure. Uniform magnetic fields along the x, y and z directions were generated by a set of four flexible-PCB coils implemented with a biplanar design[35]. The coils were attached on top and bottom faces of the insulation box with an inter-plane distance of 16 mm. The wire paths were designed using the `bfieldtools` software[36] and optimized for high field homogeneity and low stray field. Both the Teflon and the ceramic parts have 3 mm wide windows allowing optical access to the cell. The complete LWVC and oven package, shown in Fig. 2(c), is placed inside four cylindrical layers of mu-metal magnetic shielding. Transmitted light is focused onto an amplified Si photodetector (PD).

When a magnetic field is swept around zero in the x-direction, a magnetic ZFR, as the one shown in Fig. 2(b), is obtained. To obtain a signal linear around zero applied field, we sinusoidally modulate the field in the x-direction and demodulate the PD signal using a lock-in amplifier (LIA). The LIA (SRS SR830) quadrature output is digitized by a DAQ with 5MS/s sample rate for an acquisition time of $t = 0.5$ sec. Two coils are driven by a low-noise current source (Twinleaf CSB-10) to generate dc fields in the y, z directions to cancel the ambient residual field in the magnetic shield, which is a few tens of nT, and to maximize the ZFR sharpness.

As described in prior works on single-beam zero-field magnetometry[32–34], we apply a DC magnetic field component $B_x = \gamma^{-1}\omega_L\hat{x}$, where γ is the gyromagnetic ratio and ω_L is the Larmor frequency, and a parallel oscillating magnetic field $B_m = \gamma^{-1}\omega_1\cos(\omega_m t)\hat{x}$, with amplitude $\gamma^{-1}\omega_1$ and frequency ω_m, in the x-direction, transverse to the laser beam propagation. As described in Appendix A, the magnetic-field-dependent changes of the degree of spin polarization on-axis

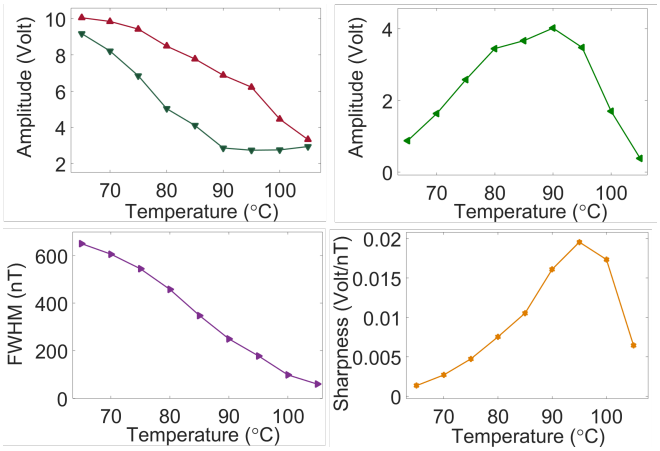

FIG. 3. ZFR parameters versus LWVC temperature, acquired with pump power of 360 µW. C.f. Fig. 2 and Eq. (1). (upper left) photodetector voltage minimum a (green) and maximum b (red) b). (upper right) amplitude $b-a$. (lower left) FWHM linewidth ΔB. (lower right) sharpness $s=(b-a)/\Delta B$, showing an optimum at 96 °C.

P_z are mapped onto the transmitted intensity, which is converted by the photodetector into an output voltage $V(B)$. This signal, as illustrated in Fig. 2(b), is well fit by the Lorentzian

$$V(B)=a+(b-a)\frac{\Delta B^2/4}{(B_x-B_0)^2+\Delta B^2/4}, \qquad (1)$$

where a is the minimum, b is the maximum, $(b-a)$ is the amplitude, B_0 is the line center that may differ from zero in case of residual uncompensated field, and ΔB is the FWHM linewidth. We use the observed amplitude and linewidth to optimize the sharpness, defined as $s=(b-a)/\Delta B$, by choice of cell temperature. As shown in Fig. 3, by increasing the temperature and thus the number density, the amplitude increases due to the higher number of atoms contributing to the ZFR signal up to a maximum value. Above this optimum, we observe a net decrease in the maximum voltage as well as in the ZFR amplitude while the FWHM linewidth decreases with number density, such that an optimum of the sharpness is obtained at 96 °C. In the low-optical-depth regime, ΔB can be related to the total magnetic relaxation rate $\Gamma=\gamma\Delta B=R_{\rm op}+\Gamma_{\rm dk}$[37], where $R_{\rm op}$ is the optical pumping rate and $\Gamma_{\rm dk}$ is the relaxation rate "in the dark". Here, however, the optical depth at 96 °C is $\mathscr{D}_0=0.9$, calculated by Eq. A3 in Appendix A, the atomic polarization inhomogeneous across the cell and the relaxation-linewidth relation is expected to be more complex.

As illustrated in Fig. 2(a), we use a LIA to demodulate the photodetector output at the same modulation frequency ω_m of the applied oscillating field B_m. In Fig. 4 (top) we show the experimental LIA quadrature output voltage for a quasi-static scan, under optimal ZFR sharpness conditions at 96 °C, and a fit to a dispersive Lorentzian profile

$$V_Q(B)=\frac{u}{2}\frac{(B-B_0)\Delta B}{(B-B_0)^2+\Delta B^2/4} \qquad (2)$$

with amplitude u. From the fit shown in Fig. 4 (top) we obtain an amplitude of $u=6.4$ V and a FWHM linewidth of

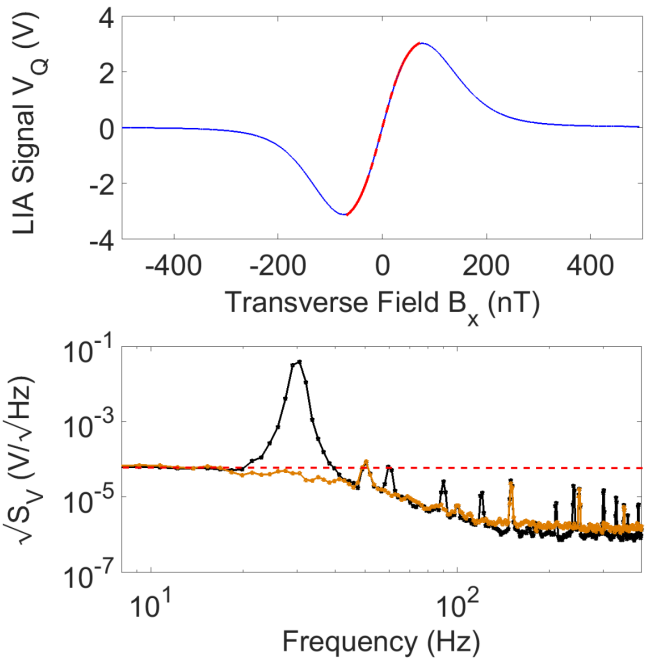

FIG. 4. LIA quadrature output signal and noise. (Top) Experimental quadrature signal $V_Q(B)$ (blue) versus transverse magnetic field B_x and fit (red) to Eq. 2. (Bottom) Amplitude spectral density (ASD) of the LIA output voltage at the zero crossing condition with (black) and without (orange) a 30 Hz reference signal. The LIA noise S_V, converted to equivalent magnetic noise using the slope of the LIA signal, implies a magnetic sensitivity of 1 pT/$\sqrt{\rm Hz}$, shown by the red dashed line, for frequencies below the LIA filter roll-off (see text).

$\Delta B=182$ nT. In Fig. 4 (bottom) we show the amplitude spectral density (ASD) obtained in V/$\sqrt{\rm Hz}$ with a FFT of the LIA signal in the time domain fed into a DAQ at the zero-crossing condition, as well as the same spectrum with a reference magnetic signal oscillating at 30 Hz with an rms amplitude of 61 pT. As in[38–40], at given detection frequency we can obtain the equivalent magnetic noise (power spectral density), as:

$$S_B=\left(\frac{dV_Q}{dB}\right)^{-2}S_V=\left(\frac{\Delta B}{2u}\right)^2 S_V \qquad (3)$$

where dV_Q/dB is the slope of the LIA quadrature signal and S_V is the power spectral noise density in V^2/Hz. We use the maximum slope, around resonance $B=B_0\approx 0$, which is equal to $dV_Q/dB=2u/\Delta B$. At 10 Hz detection frequency we found a noise level about 1 pT/$\sqrt{\rm Hz}$, calculated by using Eq. 3 with S_V from Fig. 4 (bottom) and slope from the fit in Fig. 4 (top). The roll-off of the S_V is due to a LIA 24 dB/oct low-pass filter with 1 msec time constant. We then expect a 3 dB measurement bandwidth of the OPM limited to a cutoff frequency of ≈ 160 Hz, given that the calculated relaxation rates (see Appendix A), and thus the intrinsic bandwidth of the ZFR process, are much faster.

We have described a sensitive single-beam zero-field OPM using a LWVC with a 9 mm-long Rb-vapor-filled channel of 500 µm × 500 µm cross section, buried less than 1 mm below the surface of the device. With a zero-field-resonance

technique, we demonstrate a sensitivity of $1\,\mathrm{pT}/\sqrt{\mathrm{Hz}}$ at 10 Hz that, in combination with low-frequency bandwidth and a potential sub-mm standoff distance, makes the device suitable for lab-on-chip magnetometry applications[16]. These include NMR with OPMs[41] for quantitative chemicals analysis and imaging in the zero-to-ultralow-field (ZULF) regime[41–46], plus detection of other systems such as magnetic nanoparticles[13] and magnetotactic bacteria (MTB)[47]. Possible damage of bio-samples due to operating temperatures of Rb could be reduced using Cs vapors or metastable He as well as adopting efficient on-chip thermal isolation methods[48]. The relaxation rate due to collisions with the walls could be further reduced by a higher buffer gas pressure[49] or by anti-relaxation coatings[50]. The FLICE approach to vapor cell production also enables integration of miniature vapor cells with photonic structures, such as waveguides[1].

ACKNOWLEDGMENTS

Work supported by: Spanish Ministry of Science MCIN project SAPONARIA (PID2021-123813NB-I00) and "Severo Ochoa" Center of Excellence CEX2019-000910-S; Departament de Recerca i Universitats de la Generalitat de Catalunya grant No. 2021 SGR 01453; Fundació Privada Cellex; Fundació Mir-Puig; GC, RO, and VGL acknowledge financial support from European Union NextGenerationEU (PNRR MUR project PE0000023 – NQSTI Spoke 7). MT acknowledges projects MARICHAS (PID2021-126059OA-I00) and RYC2022-035450-I financed by MCIN/AEI /10.13039/501100011033. KM acknowledges support from Grant FJC2021-047840-I funded by MCIN/AEI/10.13039/501100011033 and by the European Union project "NextGenerationEU/PRTR." Funded by the European Union (ERC, Field-Seer, 101097313). Views and opinions expressed are however those of the author(s) only and do not necessarily reflect those of the European Union or the European Research Council Executive Agency. Neither the European Union nor the granting authority can be held responsible for them.

DATA AVAILABILITY STATEMENT

The dataset that support the findings of this study are openly available in the repository `https://zenodo.org/records/10974079`.

Appendix A: optical depth and collisional rates

The intensity I of the pump beam, as it propagates through the laser-written atomic channel along the z-direction, depends on the on-axis degree of self-induced spin polarization $P_z \in [-1,1]$ via the Beer-Lambert law:

$$\frac{dI(z)}{dz} = -n\sigma(\nu)I(z)[(1-P_z(z)] \tag{A1}$$

where n is the Rb number density, $\sigma(\nu) = \pi r_e c f_{osc}^{D1} \mathscr{L}(\nu-\nu_0)$ is the absorption cross-section, r_e is the classical electron radius, c is the speed of light, $f_{osc}^{D1} \approx 0.3423$, $\mathscr{L}(\nu-\nu_0)$ is a normalized Lorentzian absorption profile with pressure-broadened FWHM linewidth Γ_L. For simplicity, we consider a homogeneous atomic polarization by neglecting the spatial distribution of $P_z(z)$ across the laser-written channel and the consequent integral over the cell length[51]. In this qualitative approach, the transmitted intensity of the pump beam, tuned near the central line of ^{85}Rb to maximize the ZFR amplitude, that reaches the photodetector is:

$$I = I_0 \exp[-n\sigma_0 l(1-P_z)] = I_0 \exp[-\mathscr{D}_0(1-P_z)] \tag{A2}$$

where I_0 is the intensity at the input of the cell and the on-resonance optical depth is given by:

$$\mathscr{D}_0 = \frac{\pi n r_e c f_{osc}^{D1} l}{\Gamma_L/2} \tag{A3}$$

where l is the atomic interaction length. With $l = l_{\mathrm{LWVC}}$, $T = 96\,^\circ\mathrm{C}$ and $\Gamma_L = 2\pi \times 13.5$ GHz, we calculate $\mathscr{D}_0 = 0.9$.

In our experimental condition, with enough buffer gas to prevent radiation trapping[29], the relaxation rate in the dark is given by:

$$\Gamma_{\mathrm{dk}} = \Gamma_{\mathrm{wd}} + \Gamma_{\mathrm{coll}}, \tag{A4}$$

where Γ_{wd} and Γ_{coll} are the depolarizing rates due to atomic diffusion to the walls and to binary collisions. The relaxation rate Γ_{wd} for the fundamental diffusion mode of a rectangular cell is[52]:

$$\Gamma_{\mathrm{wd}}^{\mathrm{LWVC}} = \left[\left(\frac{\pi}{l_x}\right)^2 + \left(\frac{\pi}{l_y}\right)^2 + \left(\frac{\pi}{l_z}\right)^2\right] \frac{D_0}{\eta} \sqrt{\frac{T(\mathrm{K})}{273.15\mathrm{K}}}, \tag{A5}$$

where $l_x = l_y = d_{\mathrm{LWVC}}$ and $l_z = l_{\mathrm{LWVC}}$ are the cavity side lengths, $D_0 = 0.12\,\mathrm{cm}^2\,\mathrm{s}^{-1}$ is the diffusion constant in 1 amg of N_2 buffer gas at 273 K[53] and η is the the nitrogen number density in amg. The collisional relaxation rate is $\Gamma_{\mathrm{coll}} = \Gamma_{\mathrm{bg}} + \Gamma_{\mathrm{se}} + \Gamma_{\mathrm{sd}}$, including Rb-buffer gas (Γ_{bg}), Rb-Rb spin-exchange (Γ_{se}) and Rb-Rb spin-destruction (Γ_{sd}) collisional rates, respectively:

$$\Gamma_{\mathrm{se}} = q_{\mathrm{se}} n \sigma_{\mathrm{se}} \bar{v}_{\mathrm{Rb\text{-}Rb}}, \tag{A6}$$

$$\Gamma_{\mathrm{sd}} = n \sigma_{\mathrm{sd}} \bar{v}_{\mathrm{Rb\text{-}Rb}}, \tag{A7}$$

$$\Gamma_{\mathrm{bg}} = n_{N_2} \sigma_{\mathrm{Rb\text{-}N_2}} \bar{v}_{\mathrm{Rb\text{-}N_2}}, \tag{A8}$$

where n (n_{N_2}) is the Rb (N_2) number density, assuming nitrogen as an ideal gas, $\bar{v}_{\mathrm{Rb\text{-}N_2}}$ ($\bar{v}_{\mathrm{Rb\text{-}Rb}}$) is the Rb-$N_2$ (Rb-Rb) relative thermal velocity, $q_{\mathrm{se}} = 5/27$ is the spin-exchange broadening factor[54], $\sigma_{\mathrm{se}} = 1.9 \times 10^{-14}\,\mathrm{cm}^2$, $\sigma_{\mathrm{sd}} = 1.6 \times 10^{-17}\,\mathrm{cm}^2$ and $\sigma_{\mathrm{Rb\text{-}N_2}} = 1 \times 10^{-22}\,\mathrm{cm}^2$ are the cross-sections for Rb-Rb spin-exchange and spin-destruction collisions and Rb-N_2 spin destruction collisions, respectively[28]. In Fig. 5 we show the nitrogen-density-dependent rates from Eqs. A5 and A8, the nitrogen-density-independent rates given by Eqs. A6 and A7, and the total collisional relaxation rate using Eq. A4, all calculated at $T = 96\,^\circ\mathrm{C}$. At our experimental density of

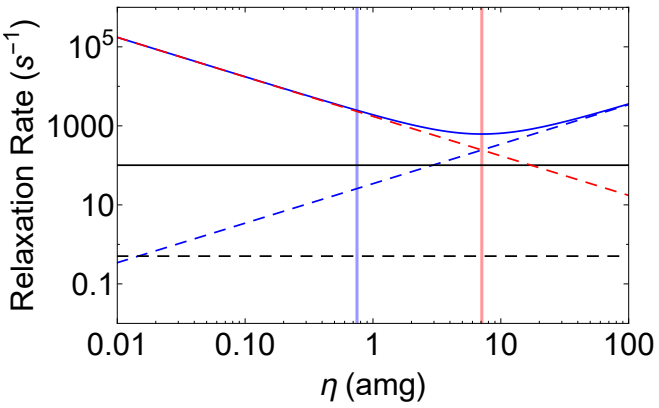

FIG. 5. Collisional relaxation rates as a function of N_2 buffer gas density at $T = 96\,^{\circ}$C. Γ_{wd}^{LWVC} (dashed red), Γ_{bg} (dashed blue), Γ_{sd} (dashed black), Γ_{se} (continuous black), total Γ_{dk} (continuous blue). Experimental (optimal) nitrogen density is indicated with a vertical blue (red) line at 0.75 amg (7.1 amg).

$\eta = 0.75$ amg, we obtain a dominant contribution due to collisions with the walls $\Gamma_{wd}^{LWVC} = 2\pi \times 2326\ s^{-1}$, a spin-exchange rate $\Gamma_{se} = 2\pi \times 111.2\ s^{-1}$, Rb-buffer gas and spin-destruction rates $\Gamma_{bg} = 2\pi \times 25.7\ s^{-1}$ and $\Gamma_{sd} = 2\pi \times 0.5\ s^{-1}$, respectively, and a total rate in the dark of $\Gamma_{dk} = 2\pi \times 2483\ s^{-1}$. An optimum of $\eta_{opt} = 7.1$ amg would correspond to a minimum total rate of $\Gamma_{dk} = 2\pi \times 600\ s^{-1}$. The on-resonance local rate of optical pumping is:

$$R_{op} = \sigma_0 \phi_{phot} = \frac{r_e c f_{osc}^{D1}}{\Gamma_L/2} \frac{I_{pump}}{\hbar \omega_{pump}} \tag{A9}$$

where $\omega_{pump} = 2\pi \times 3.77 \times 10^{14}$ Hz, ϕ_{phot} is the photon flux, $I_{pump} = P_{pump}/(\pi w^2/2)$ is the pump intensity for a Gaussian beam with radius w and power P_{pump}. Before atomic interaction and beam focusing into the sensing channel, we measured a power of 360 µW for a beam radius of $w \sim 1$ mm. However, given a room-temperature experimental transmission of about 15% through the laser-written channel, in Eq. A9 we use $P_{pump} = 55$ µW and we obtain $R_{op} = 2\pi \times 1513\ s^{-1}$. This rate is overestimated due to the assumption of homogeneous polarization and pump intensity across the cell in Eq. A9.

Appendix B: projected sensitivity versus sensing volume

While technical and optical noise sources often prevent to achieve atomic-noise-limited sensor performance, in the context of miniaturized atomic sensors, as the described LWVC with sub-mm dimensions, we can gain insights on the dependence on sensing volume V, by calculating the projected magnetic sensitivity due to atomic shot noise (ASN)[33,55]:

$$\delta B_{ASN} = \frac{1}{\gamma}\sqrt{\frac{2e\Gamma_{dk}}{N_{at}t}} = \frac{1}{\gamma}\sqrt{\frac{2e\Gamma_{dk}}{nVt}} \tag{B1}$$

where $N_{at} = nV$ is the total number of atoms and t is the measurement time. By using the relaxation rate in the dark Γ_{dk}, already defined in Eq. A4, we neglect optically-induced relaxation effects, which can be significantly reduced in other types of sensitive magnetometers, as those based on free-induction-decay (FID) and off-resonance probing[38,56]. At given operating temperature T and volume, thus fixed geometrical parameters in the rate due to diffusion to the walls Γ_{wd}, one can find the buffer gas density that minimizes both Γ_{dk} and the projected sensitivity through Eq. B1. This value typically corresponds to the crossing point between Γ_{wd}, which decreases with increased N_2 pressure and Γ_{bg}, which in contrast increases with the nitrogen density, as shown in Fig. 5. For the sensing volume of the laser-written channel used in this experiment $V_{LWVC} = d_{LWVC}{}^2 \times l_{LWVC} = 2.25\ mm^3$, and working temperature of $T = 96\,^{\circ}$C, optimal for the ZFR sharpness, the optimal buffer gas density corresponds to $\eta_{opt} = 7.1$ amg, which gives a projected magnetic sensitivity of 18.3 fT/$\sqrt{\text{Hz}}$, calculated by using Eq. B1 with $t = 0.5$ sec. As illustrated in Fig. 5, for our experimental condition of $\eta = 0.75$ amg the relaxation rate due to alkali-walls collisions Γ_{wd}^{LWVC} is nonetheless significantly decreased, resulting in a projected ASN-limited sensitivity of 36.6 fT/$\sqrt{\text{Hz}}$. In practice, ZFR-OPMs as the described magnetometer, present additional optical and technical noise[33,34].

[1] M. T. Hummon, S. Kang, D. G. Bopp, Q. Li, D. A. Westly, S. Kim, C. Fredrick, S. A. Diddams, K. Srinivasan, V. Aksyuk, and J. E. Kitching, Optica **5**, 443 (2018).
[2] S. Knappe, V. Shah, P. D. D. Schwindt, L. Hollberg, J. Kitching, L.-A. Liew, and J. Moreland, Applied Physics Letters **85**, 1460 (2004).
[3] R. Cipolletti, J. Riedrich-Moeller, T. Fuchs, A. Wickenbrock, and D. Budker, in 2021 IEEE Sensors (2021) pp. 1–4.
[4] S. Chen, D. J. Reed, A. R. MacKellar, L. A. Downes, N. F. A. Almuhawish, M. J. Jamieson, C. S. Adams, and K. J. Weatherill, Optica **9**, 485 (2022).
[5] W. C. Griffith, S. Knappe, and J. Kitching, Opt. Express **18**, 27167 (2010).
[6] R. Jiménez-Martínez and S. Knappe, "Microfabricated Optically-Pumped Magnetometers," in High Sensitivity Magnetometers, edited by A. Grosz, M. J. Haji-Sheikh, and S. C. Mukhopadhyay (Springer International Publishing, Cham) pp. 523–551.
[7] M. Jiang, H. Zhai, C. Jiang, J. Wang, C. Chen, Q. Zhang, D. Wu, B. Zhang, Z. Zeng, J. Lin, Y. Wang, and P. Jin, Applied Physics Letters **123**, 062406 (2023).
[8] M. P. Ledbetter, I. M. Savukov, D. Budker, V. Shah, S. Knappe, J. Kitching, D. J. Michalak, S. Xu, and A. Pines, Proceedings of the National Academy of Sciences **105**, 2286–2290 (2008).
[9] D. J. Kennedy, Progress in Microfluidic Nuclear Magnetic Resonance, Ph.D. thesis, UC Berkeley (2014).
[10] J. Eills, W. Hale, and M. Utz, Progress in Nuclear Magnetic Resonance Spectroscopy **128**, 44–69 (2022).
[11] D. Faivre and D. Schüler, Chemical Reviews **108**, 4875 (2008).
[12] C. L. Monteil, D. Vallenet, N. Menguy, K. Benzerara, V. Barbe, S. Fouteau, C. Cruaud, M. Floriani, E. Viollier, G. Adryanczyk, N. Leonhardt, D. Faivre, D. Pignol, P. López-García, R. J. Weld, and C. T. Lefevre, Nature Microbiology **4**, 1088 (2019).
[13] M. Jofre, J. Romeu, and L. Jofre-Roca, New Journal of Physics **25**, 013028 (2023).
[14] S. Xu, M. H. Donaldson, A. Pines, S. M. Rochester, D. Budker, and V. V. Yashchuk, Applied Physics Letters **89** (2006).
[15] M. Hoese, M. K. Koch, V. Bharadwaj, J. Lang, J. P. Hadden, R. Yoshizaki, A. N. Giakoumaki, R. Ramponi, F. Jelezko, S. M. Eaton, and A. Kubanek, Phys. Rev. Appl. **15**, 054059 (2021).
[16] R. D. Allert, F. Bruckmaier, N. R. Neuling, F. A. Freire-Moschovitis, K. S. Liu, C. Schrepel, P. Schätzle, P. Knittel, M. Hermans, and D. B. Bucher, Lab Chip **22**, 4831 (2022).
[17] M. W. Mitchell and S. Palacios Alvarez, Rev. Mod. Phys. **92**, 021001 (2020).

[18] N. Bellini, K. C. Vishnubhatla, F. Bragheri, L. Ferrara, P. Minzioni, R. Ramponi, I. Cristiani, and R. Osellame, Opt. Express **18**, 4679 (2010).

[19] A. Schaap, T. Rohrlack, and Y. Bellouard, Lab Chip **12**, 1527 (2012).

[20] R. Memeo, P. Paiè, F. Sala, M. Castriotta, C. Guercio, T. Vaccari, R. Osellame, A. Bassi, and F. Bragheri, Journal of biophotonics **14**, e202000396 (2021).

[21] V. G. Lucivero, A. Zanoni, G. Corrielli, R. Osellame, and M. W. Mitchell, Opt. Express **30**, 27149 (2022).

[22] A. Marcinkevičius, S. Juodkazis, M. Watanabe, M. Miwa, S. Matsuo, H. Misawa, and J. Nishii, Opt. Lett. **26**, 277 (2001).

[23] R. Osellame, H. Hoekstra, G. Cerullo, and M. Pollnau, Laser & Photonics Reviews **5**, 442 (2011).

[24] G. Corrielli, A. Crespi, and R. Osellame, Nanophotonics **10**, 3789 (2021).

[25] E. Pelucchi, G. Fagas, I. Aharonovich, D. Englund, E. Figueroa, Q. Gong, H. Hannes, J. Liu, C.-Y. Lu, N. Matsuda, J.-W. Pan, F. Schreck, F. Sciarrino, C. Silberhorn, J. Wang, and K. D. Jöns, Nature Reviews Physics **4**, 194 (2022).

[26] We performed leak tests with different epoxy-sealed cells, observing no leaking up to 150 °C.

[27] M. V. Romalis, E. Miron, and G. D. Cates, Phys. Rev. A **56**, 4569 (1997).

[28] S. J. Seltzer, Developments in Alkali-Metal Atomic Magnetometry, Ph.D. thesis, Princeton University (2008).

[29] M. A. Rosenberry, J. P. Reyes, D. Tupa, and T. J. Gay, Phys. Rev. A **75**, 023401 (2007).

[30] T. Scholtes, S. Woetzel, R. IJsselsteijn, V. Schultze, and H.-G. Meyer, Applied Physics B **117**, 211 (2014).

[31] S. Dyer, A. McWilliam, D. Hunter, S. Ingleby, D. P. Burt, O. Sharp, F. Mirando, P. F. Griffin, E. Riis, and J. P. McGilligan, Applied Physics Letters **123**, 074001 (2023).

[32] J. Dupont-Roc, S. Haroche, and C. Cohen-Tannoudji, Physics Letters A **28**, 638 (1969).

[33] V. Shah, S. Knappe, P. D. D. Schwindt, and J. Kitching, Nature Photonics **1**, 649 (2007).

[34] S. P. Krzyzewski, A. R. Perry, V. Gerginov, and S. Knappe, Journal of Applied Physics **126**, 044504 (2019).

[35] M. C. D. Tayler, K. Mouloudakis, R. Zetter, D. Hunter, V. G. Lucivero, S. Bodenstedt, L. Parkkonen, and M. W. Mitchell, Phys. Rev. Appl. **18**, 014036 (2022).

[36] R. Zetter, A. J. Mäkinen, J. Iivanainen, K. C. J. Zevenhoven, R. J. Ilmoniemi, and L. Parkkonen, Journal of Applied Physics **128** (2020).

[37] N. Castagna and A. Weis, Phys. Rev. A **84**, 053421 (2011).

[38] V. Gerginov, S. Krzyzewski, and S. Knappe, J. Opt. Soc. Am. B **34**, 1429.

[39] R. Jiménez-Martínez, W. C. Griffith, S. Knappe, J. Kitching, and M. Prouty, J. Opt. Soc. Am. B **29**, 3398.

[40] C. Troullinou, V. G. Lucivero, and M. W. Mitchell, Phys. Rev. Lett. **131**, 133602 (2023).

[41] M. P. Ledbetter, I. Savukov, S. J. Seltzer, and D. Budker, "Detection of nuclear magnetic resonance with atomic magnetometers," in Optical Magnetometry, edited by D. Budker and D. F. Jackson Kimball (Cambridge University Press, 2013) p. 265–284.

[42] V. S. Bajaj, J. Paulsen, E. Harel, and A. Pines, Science **330**, 1078 (2010).

[43] R. Jiménez-Martínez, D. J. Kennedy, M. Rosenbluh, E. A. Donley, S. Knappe, S. J. Seltzer, H. L. Ring, V. S. Bajaj, and J. Kitching, Nature Communications **5**, 3908 (2014).

[44] T. Theis, P. Ganssle, G. Kervern, S. Knappe, J. Kitching, M. P. Ledbetter, D. Budker, and A. Pines, Nature Physics **7**, 571 (2011).

[45] L. Chuchkova, S. Bodenstedt, R. Picazo-Frutos, J. Eills, O. Tretiak, Y. Hu, D. A. Barskiy, J. de Santis, M. C. D. Tayler, D. Budker, and K. F. Sheberstov, The Journal of Physical Chemistry Letters **14**, 6814 (2023).

[46] K. Mouloudakis, S. Bodenstedt, M. Azagra, M. W. Mitchell, I. Marco-Rius, and M. C. D. Tayler, The Journal of Physical Chemistry Letters **14**, 1192 (2023).

[47] I. S. M. Khalil, M. P. Pichel, L. Zondervan, L. Abelmann, and S. Misra, "Characterization and control of biological microrobots," in Experimental Robotics: The 13th International Symposium on Experimental Robotics, edited by J. P. Desai, G. Dudek, O. Khatib, and V. Kumar (Springer International Publishing, Heidelberg, 2013) pp. 617–631.

[48] F. Ceccarelli, S. Atzeni, A. Prencipe, R. Farinaro, and R. Osellame, J. Lightwave Technol. **37**, 4275 (2019).

[49] A. G. Ciriolo, R. M. Vázquez, V. Tosa, A. Frezzotti, G. Crippa, M. Devetta, D. Faccialá, F. Frassetto, L. Poletto, A. Pusala, C. Vozzi, R. Osellame, and S. Stagira, Journal of Physics: Photonics **2**, 024005 (2020).

[50] G. Vasilakis, H. Shen, K. Jensen, M. Balabas, D. Salart, B. Chen, and E. S. Polzik, Nature Physics **11**, 389 (2015).

[51] Y. Ito, D. Sato, K. Kamada, and T. Kobayashi, Opt. Express **24**, 15391 (2016).

[52] J. Kitching, Applied Physics Reviews **5**, 031302 (2018).

[53] Obtained from the value $D_0 = 0.16\,\mathrm{cm}^2\,\mathrm{s}^{-1}$ measured in ^{57} at $T_0 = 60\,^\circ\mathrm{C}$ using the scaling $D \propto (T(\mathrm{K})/T_0(\mathrm{K}))^{3/2}$[58].

[54] For simplicity we neglect spin-exchange collisions between the two Rb isotopes and we use the spin-exchange broadening factor for ^{85}Rb, obtained with nuclear spin $I = 5/2$ in[28].

[55] D. Sheng, S. Li, N. Dural, and M. V. Romalis, Phys. Rev. Lett. **110**, 160802 (2013).

[56] M. Limes, E. Foley, T. Kornack, S. Caliga, S. McBride, A. Braun, W. Lee, V. Lucivero, and M. Romalis, Phys. Rev. Appl. **14**, 011002 (2020).

[57] K. Ishikawa and T. Yabuzaki, Phys. Rev. A **62**, 065401 (2000).

[58] V. G. Lucivero, N. D. McDonough, N. Dural, and M. V. Romalis, Phys. Rev. A **96**, 062702 (2017).